A Broadband Fluorographene Photodetector

Sichao Du, Wei Lu, Ayaz Ali, Pei Zhao, Khurram Shehzad, Hongwei Guo, Lingling Ma, Xuemei Liu, Xiaodong Pi, Peng Wang, Hehai Fang, Zhen Xu, Chao Gao, Yaping Dan, Pingheng Tan, Hongtao Wang, Cheng-Te Lin, Jianyi Yang, Shurong Dong, Zhiyuan Cheng, Erping Li, Wenyan Yin, Jikui Luo, Bin Yu, Tawfique Hasan, Yang Xu,* Weida Hu,* and Xiangfeng Duan

High-performance photodetectors operating over a broad wavelength range from ultraviolet, visible, to infrared are of scientific and technological importance for a wide range of applications. Here, a photodetector based on van der Waals heterostructures of graphene and its fluorine-functionalized derivative is presented. It consistently shows broadband photoresponse from the ultraviolet (255 nm) to the mid-infrared (4.3 µm) wavelengths, with three orders of magnitude enhanced responsivity compared to pristine graphene photodetectors. The broadband photodetection is attributed to the synergistic effects of the spatial nonuniform collective quantum confinement of sp^2 domains, and the trapping of photoexcited charge carriers in the localized states in sp^3 domains. Tunable photoresponse is achieved by controlling the nature of sp^3 sites and the size and fraction of sp^3/sp^2 domains. In addition, the photoresponse due to the different photoexcited-charge-carrier trapping times in sp^2 and sp^3 nanodomains is determined. The proposed scheme paves the way toward implementing high-performance broadband graphene-based photodetectors.

Photodetectors as a class of optoelectronics device have been widely employed in diverse fields, including spectroscopy,[1] telecommunication,[2] astronomy,[3] agriculture,[4] pharmaceuticals,[5] and environmental monitoring.[6] In contrast to photodetectors operating at a specific wavelength range, broadband photodetectors with photoresponse to a much wider spectrum and spectrally distinctive are highly desirable, owing to their importance to a variety of applications.[7,8] The wealth of sufficient information held in the broad spectral domain offers advantages over traditional panchromatic and multispectral imagery.[9] Hence, hyperspectral imaging has been used as a powerful technique for global climate research, mapping of wetlands, mineral

Dr. S. Du, W. Lu, A. Ali, Dr. K. Shehzad, H. Guo, L. Ma, X. Liu, Prof. J. Yang, Prof. S. Dong, Prof. Z. Cheng, Prof. E. Li, Prof. W. Yin, Prof. J. Luo, Prof. Y. Xu
College of Information Science and Electronic Engineering
Zhejiang University
Hangzhou, Zhejiang 310027, China
E-mail: yangxu-isee@zju.edu.cn

Prof. P. Zhao, Prof. H. Wang
Institute of Applied Mechanics
Zhejiang University
Hangzhou, Zhejiang 310027, China

Dr. S. Du, Prof. Y. Xu, Prof. X. Pi
State Key Laboratory of Silicon Materials
College of Material Science
Zhejiang University
Hangzhou, Zhejiang 310027, China

P. Wang, H. Fang, Prof. W. Hu
National Laboratory for Infrared Physics
Shanghai Institute of Technical Physics
Chinese Academy of Sciences
Shanghai 200083, China
E-mail: wdhu@mail.sitp.ac.cn

Dr. Z. Xu, Prof. C. Gao
MOE Key Laboratory of Macromolecular
Synthesis and Functionalization
Zhejiang University
Hangzhou, Zhejiang 310027, China

Prof. Y. Dan
University of Michigan - Shanghai Jiao Tong University Joint Institute
Shanghai Jiao Tong University
Shanghai 200240, China

Prof. P. Tan
State Key Laboratory of Superlattices and Microstructures
Institute of Semiconductors
Chinese Academy of Sciences
Beijing 100083, China

Prof. C.-T. Lin
Key Laboratory of Marine Materials and Related Technologies
Zhejiang Key Laboratory of Marine Materials and Protective Technologies
Ningbo Institute of Materials Technology and Engineering
Chinese Academy of Sciences
Ningbo, Zhejiang 315201, China

Prof. B. Yu
College of Nanoscale Science and Engineering
State University of New York
New York, NY 12203, USA

Dr. T. Hasan
Department of Engineering
University of Cambridge
Cambridge CB3 0FA, UK

Prof. X. Duan
Department of Chemistry and Biochemistry
University of California
Los Angeles, CA 90095, USA

**ADVANCED
SCIENCE NEWS**

www.advancedsciencenews.com

**ADVANCED
MATERIALS**

www.advmat.de

identification, crop analysis, bathymetry, etc.[10] In addition, two-color intelligent detection and recognition has also been under extensive investigation. For instance, UV–vis photodetectors can meet the demands on astronomical detection,[11] wide spectral switches,[12] or memory storage;[13] vis and near-infrared (IR) photodetectors are widely used in consumer electronics,[14] video recording,[15] and remote sensing;[16] multiband mid-IR photodetectors have attracted interest due to their numerous exciting applications, such as in surveillance,[17] medical diagnostics,[18] bioimaging,[4] and navigational aids.[19]

However, studies on photodetectors have mainly focused on their performance under a specific wavelength range (UV, vis, or IR). Broadband photodetectors generally have a complicated system configuration with high cost, consisting of trichroic prisms, optical filters, charge coupled devices, etc.[20] Graphene has been considered as a promising material for ultra-broadband photodetectors as its absorption spectrum covers the entire UV to terahertz wavelengths.[21] However, the photoresponsivity of pristine graphene photodetectors is insufficient due to the low absorption efficiency of incident photons and the short lifetime of photoexcited carriers.[22] Furthermore, its semimetal behavior results in substantial dark currents on account of the absence of an intrinsic gap, which is not suitable for highly responsive photodetectors.[23] Hence, efforts have been made to fabricate graphene with plasmonic nanostructures,[24] microcavities,[25] silicon waveguide,[26] transition-metal dichalcogenide stacks,[27] and hybridized quantum dots.[28] Despite the excellent improved photoresponsivity, light absorption either relies on the materials, structures, or resonant frequencies, thus still restricting the broadband spectral photodetection. Therefore, the challenge to enhance the photoresponse without sacrificing the broadband characteristics still remains.

Here, we present a wide-broadband photodetector composed of graphene and its fluorine-functionalized derivative. In contrast to other graphene-based photodetectors, the van der Waals heterostructure efficiently improves the device performance while keeping the broadband photoresponse of graphene. The rehybridization of carbon with fluorine results in a mixture of sp^2 and sp^3 nanodomains, inducing a series of discrete quantum-confined states and a number of structural localized states for trapping of photoexcited charge carriers. Tunable photoresponse has been achieved by modulating the dihedral angles of sp^3 sites, and the size/shape and fraction of sp^3/sp^2 domains. The photocurrent due to the different photoexcited-charge-carrier trapping times in sp^2 and sp^3 nanodomains has been distinguished. Furthermore, we demonstrate a prototype device yielding exceptional photoresponsivities over a wide-broad spectral range.

Fluorine has been demonstrated to alter pristine graphene from a conductive semimetal to insulator (bandgap from 0 to 4.1 eV).[29] Since sp^2 hybridized carbon atom in graphene has a p_z orbital in the direction perpendicular to the basal plane forming a π and conjugated π^* bond, when fluorine adatoms are adsorbed on the surface, they form covalent bonds with the carbon atoms which are rehybridized from trigonal sp^2 to tetragonal sp^3 bonds.[30] Such a transformation results in an opening of a bandgap through the removal of bands near the Fermi level of pristine graphene. Depending on the degree of fluorination, there is a certain fraction of carbon rehybridized to

sp^3 and bonded with fluorine. The remaining carbon is still sp^2 bonded with neighboring carbon atoms. This atomic and electronic feature of fluorographene with variable sp^3/sp^2 fractions offers novel functionalities for photodetectors. Therefore, we fabricated a fluorographene/graphene (FG/Gr) photodetector with an FG layer on the top of a graphene layer contacting with electrodes as shown in **Figure 1**a.

To explore the functionalities brought from the FG, photoluminescence (PL) measurements were carried out at different laser excitation wavelengths. As exhibited in Figure 1d, it can be observed that under 300 and 350 nm laser excitations, the PL peaks are at 518 nm. The intensity of the PL under 350 nm excitation is higher than that under 300 nm excitation. The PL peak shifts to longer wavelength as the excitation wavelength increases from 350 to 450 nm. Since there is a nonuniform coverage of fluorine, the FG can be described as a 2D network of sp^2 C−C domains isolated within the sp^3 C−F$_x$ matrix (x represents the atomic ratio between C and F indicating the coverage of fluorine), or vice versa as shown in Figure 1b. From the Raman results (Figure S1, Supporting Information), the average size of the sp^3 domains can be estimated from 5.34 to 13.73 nm by:[31]

$$L_a(\text{nm}) = (2.4 \times 10^{-10})\lambda(\text{nm})^4 \left(\frac{I_D}{I_G}\right)^{-1} \tag{1}$$

The optoelectronic properties are thus mainly determined by the π and π^* states of sp^2 domains, which lie within the σ–σ^* states of sp^3 domains.[32] The energy gap between π and π^* states generally depends on the size of the sp^2 domain and the conjugation length. A number of sp^3 rehybridized induced localized states n, which is related to the dihedral angle of the σ bonds, exist in the band tail of the π and π^* states or lie deeper within the π–π^* gap.[33] Therefore, the PL peak at 518 nm is ascribed to an overall π and π^* transition (2.39 eV) from the sp^2 domains with a Stokes' shift of 168 nm (1.15 eV). As the excitation wavelength increases, the PL spectrum gets broader and shifts to the longer wavelength due to n–π transitions from sp^3 domains as depicted in Figure 1c. The former emission bears the discrete feature due to quantum confinement of electrons inside the sp^2 domains.[34] The latter emission possesses broad absorption and emission states band within the π–π^* gap.

The photocurrent measurements of a reference Gr/Gr device and the FG/Gr device were then conducted and compared at different laser wavelengths with a fixed irradiance (**Figure 2**a,b and Figure S2a,b, Supporting Information). The photocurrent ΔI of FG/Gr increases from nA to µA, with over 1000 times increase compared to Gr/Gr. Figure 2c,d shows the responsivity of these two photodetectors as a function of incident laser irradiance at different laser wavelengths. The responsivity of FG/Gr decreases with respect to the increase of laser irradiance. It is worth mentioning that we have tested a number of FG/Gr devices and the statistical responsivities at different laser wavelengths are exhibited in **Figure 3**a–i. The observed photoresponse can be explained by the operating principle and energy band structure. When the FG/Gr heterostructure is illuminated by light, the electrons in the π state could be excited forming

ADVANCED
SCIENCE NEWS
www.advancedsciencenews.com

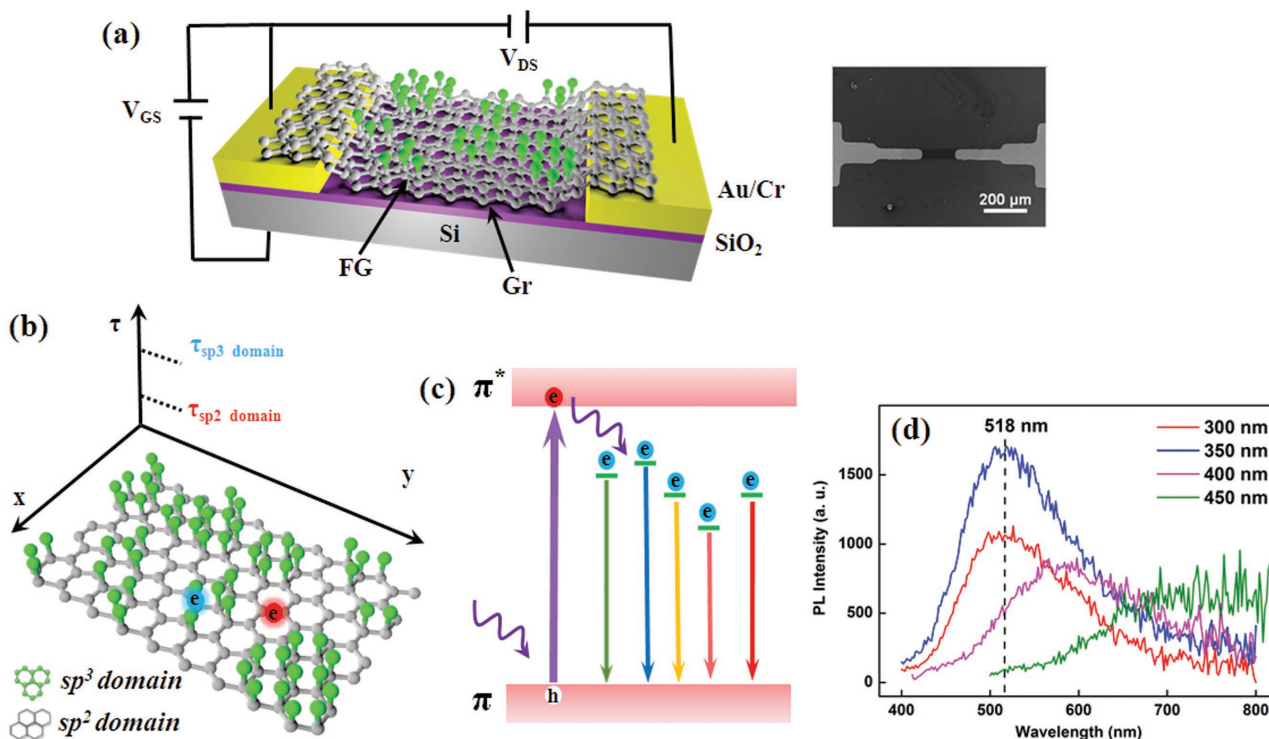**ADVANCED**
MATERIALS
www.advmat.de

Figure 1. Device structure and PL characterization. a) Schematic FG/Gr photodetector structure and the top-view SEM image. b,c) Schematic sp^3 and sp^2 domains on FG with indicated trapped carrier lifetime (b) and corresponding optical transitions (c). d) PL spectra of the FG at different excitation wavelengths.
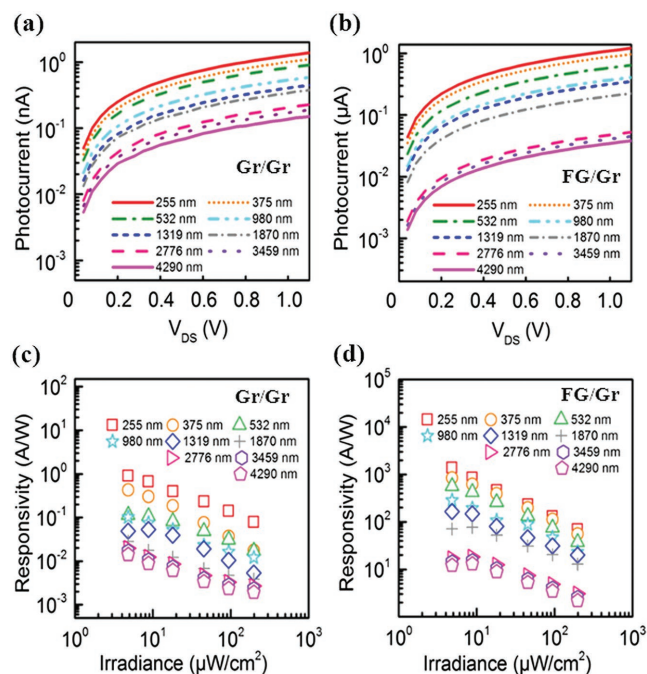

Figure 2. Photoresponse results. a,b) The photocurrent ΔI as a function of V_{DS} of Gr/Gr (a) and FG/Gr (b) devices at different laser wavelengths with a fixed irradiance of 198 µW cm^{-2}. c,d) Responsivity as a function of the laser irradiance of Gr/Gr (c) and FG/Gr (d) devices at different laser wavelengths with $V_{DS} = 1$ V and $V_{GS} = 28$ V.

electron–hole pairs. The presence of quantum confinement and localized states in the π–$\pi*$ gap leads to the trapping of these electrons, while the holes flow into the graphene channel via the built-in potential at the FG/Gr heterostructure junction, resulting in the photoinduced current.

The measured photoresponse characteristics manifest a broadband detection, where the FG/Gr devices show strong photoresponse in the whole tested wavelength range from 255 nm to 4.3 µm. The responsivity of the FG/Gr photodetector is more than three orders of magnitude higher than that of the Gr/Gr photodetector. Since various sizes/shapes of the sp^2 domains induce spatial nonuniform quantum confinements, a series of discrete quantum-confined states from the sp^2 domains contribute to the broadband photoresponse. Furthermore, for longer wavelength, the charge carriers generated at lower energy distribution cannot be excited to the relatively high $\pi*$ states. Instead, the excited carriers are mainly trapped in the localized states in sp^3 domains, contributing the broadband photoresponse. We should point out that the performance of our FG/Gr photodetector has not been fully optimized yet. We expect that the device would also further respond to the wavelengths below 255 nm and above 4.3 µm.

Furthermore, the photocurrent and dark current can be smoothly tuned by varying the back-gate voltage V_{GS} (Figure S3a, Supporting Information). The transfer of photogenerated holes from FG to graphene induces p-type doping, which leads to an upshift of the V_{Dirac} of FG/Gr of $\approx$30 V compared to Gr/Gr. Figure S3b (Supporting Information) clearly shows linear characteristics of I_{DS}–V_{DS} at all V_{GS} tuned from 0 to 25 V,

ADVANCED
SCIENCE NEWS
www.advancedsciencenews.com
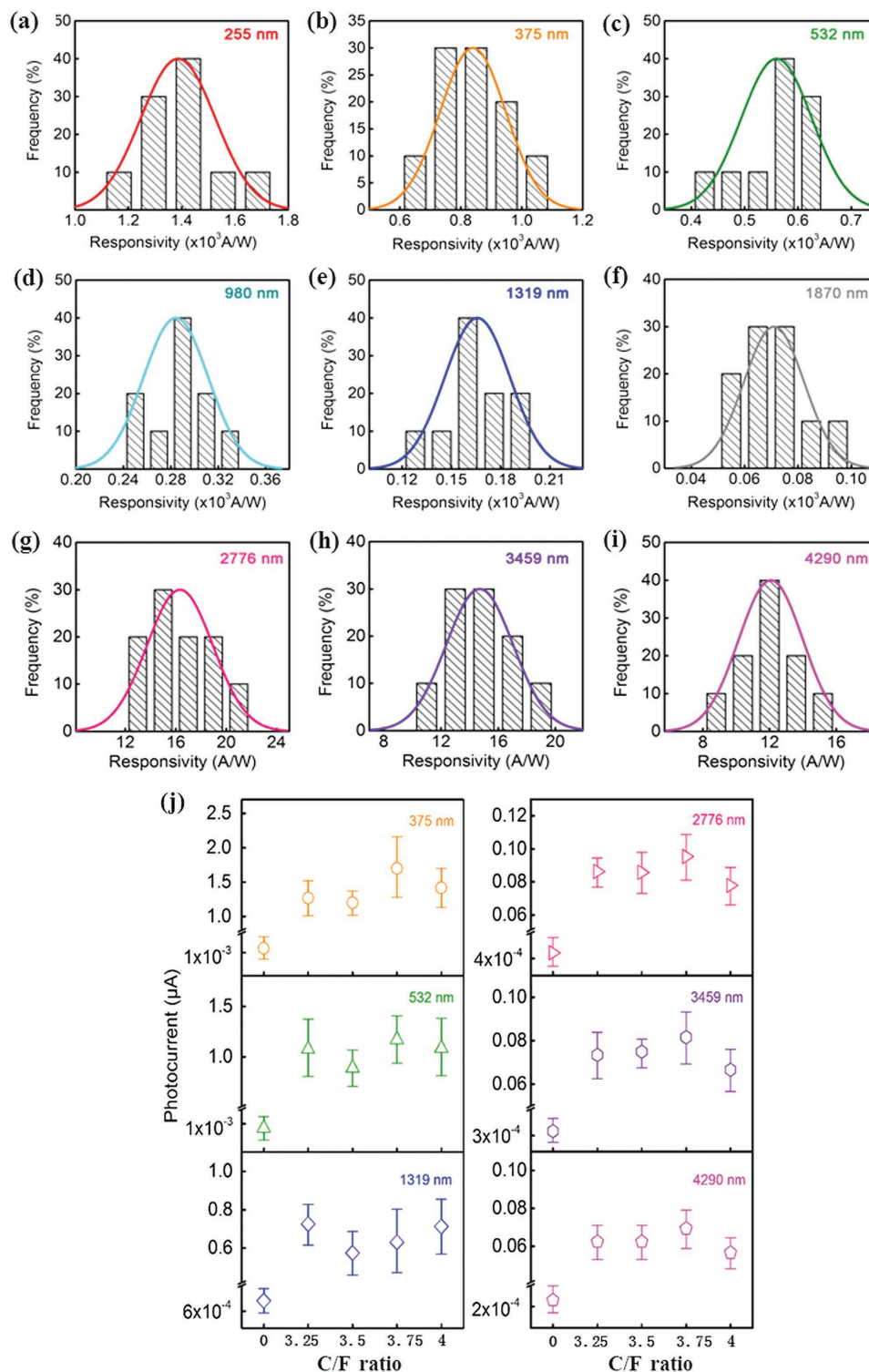
ADVANCED
MATERIALS
www.advmat.de

Figure 3. Statistical responsivities. Frequency of responsivity at: a) 255, b) 375, c) 532, d) 980, e) 1319, f) 1870, g) 2776, h) 3459, and i) 4290 nm laser wavelengths of FG/Gr devices with 3.75 C/F ratio; the laser irradiance was 4.83 μW cm^{-2} (11 mW cm^{-2} for mid-IR lasers), $V_{DS} = 1$ V, $V_{GS} = 28$ V. j) Photocurrent as a function of the C/F ratio at these laser wavelengths with a irradiance of 198 μW cm^{-2} (11 mW cm^{-2} for mid-IR lasers), where the zero represents Gr/Gr device and the error bar indicates the variance of multiple devices of the same type.

indicating an Ohmic contact instead of a Schottky contact of the FG/Gr device. The photocurrent at different laser wavelengths, as a function of C/F ratio x, is displayed in Figure 3j, where

zero indicates the Gr/Gr device. It should be noted that we have tested tens of devices and the variance of measured data is shown in the figure. As the C/F ratio decreases, more fluorine

**ADVANCED
SCIENCE NEWS**

www.advancedsciencenews.com

**ADVANCED
MATERIALS**

www.advmat.de

adatoms bonded with the carbon atoms, leads to a higher degree of sp^3 rehybridization. A larger coverage of fluorine leads to a greater number of the quantum-confined sp^2 nanodomains and the localized states in the sp^3 nanodomains, thus leading to a higher responsivity. However, a characteristic photoresponse saturation was observed at 3.75 C/F ratio, where the resulting sp^2/sp^3 nanodomains achieve their optimal size and number for the trapping of photoexcited electrons. Since the overall C/F ratio obtained from the X-ray photoelectron spectroscopy (XPS) results is 4, the density of F atoms in the FG/Gr device can be calculated to be 4.75×10^{14} cm^{-2}. In addition, a characteristic saturation of responsivity with the decrease of C/F ratio was observed. The effective absorption becomes saturated as the number of C−F bonds reaches its limit on the FG, where the absorption constant η is estimated to be 0.02 in a similar condition as reported previously.[35] Under illumination, trapped electrons in the FG form an electric field in the direction opposite to the gate electric field, inducing the photogating effect.[36] Since the size and shape of sp^2 and sp^3 domains are random on FG, resulting in a local nonuniformity of the electric field, we believe that the spatial nonuniformity of the photogating effect could be further improved to obtain a higher photoresponse.

It is reported that the photoresponse is also attributed to other mechanisms simultaneously, including photo-thermoelectric (PTE),[37] bolometric (BOL),[38] and hot-carrier effects.[39] To obtain insight into the potential contributions from thermal effects, including the PTE effect from the Au/Cr electrodes and the BOL effect from FG/Gr, we calculated the responsivity (R) from these two effects by:

i) $R_{PTE} \approx S_M (\Delta T / P_{opt}) G$, where the Seebeck coefficient S_M is given by:

$$S_M = -\frac{\pi^2 k^2 T}{3q} \frac{1}{G} \frac{dG}{dV_{GS}} \left(\frac{dV_{GS}}{dE} \right)_{E=E_F} \quad (2)$$

and the temperature difference at the junction is $\Delta T = P\alpha/k2\pi h$; P_{opt} is the optical power, and G is the conductance, I_{DS}/V_{DS}. R_{PTE} can then be estimated as 9.8×10^{-25} A W^{-1};

ii) $R_{BOL} = (E_a/kT^2)(\Delta T/P_{opt}) \approx 1.7 \times 10^{-4}$ A W^{-1}, where E_a is the activation energy.

Both R_{PTE} and R_{BOL} are far from the responsivity of the FG/Gr photodetector we obtained experimentally, as shown in Figure 2d; also, the hot-carrier multiplications contributing to the responsivity are negligible, and this will be discussed in the following section. We can thus rule out the contributions from these mechanisms for generating photocurrent in our case. Moreover, it is also informative to consider a nontrap case. The density of photoexcited electrons and holes is $\Delta n = \Delta p = \phi \tau_l$, where ϕ is the photon flux and τ_l is the carrier lifetime in graphene. The photocurrent can be calculated from $I_{ph} = (W/L)V_{DS}\Delta\sigma$, where W and L are the width and length of the graphene channel, the change of conductivity from $\Delta\sigma = q(\mu_n + \mu_p)\Delta p$; q is the electron charge and μ_n and μ_p are the electron and hole mobility. The nontrap responsivity $R_{nontrap}$ can then be obtained as 2.46×10^{-5} A W^{-1}.

Therefore, we believe that the photoresponse of the FG/Gr device is ascribed to photogating effects in both sp^2 and sp^3 domains. The total responsivity R consists of these two

contributions R_{sp^2} and R_{sp^3}, with a 6.4 R_{sp^3}/R_{sp^2} ratio. As discussed in the previous sections, the trapping of photoexcited electrons in sp^2 and sp^3 domains is due to the quantum confinement and localized states, respectively, where the trapping time τ_{sp^3} is longer than τ_{sp^3} as indicated in Figure 1b. The trapped charge density at saturation is determined by[40] $N_{sat} = \phi_{sat}\tau_S$, where the absorbed photon flux is $\varphi = \eta P_{laser}\lambda/Ahc$, and τ_S is the dominant time constant from both sp^2 and sp^3 domains. η is the absorption coefficient, A is the area of illumination, h is Planck's constant, and c is the speed of light. The trapped charge density of FG at saturation N_{sat} is then calculated to be 9.8×10^{14} cm^{-2}.

Since the photocurrent is defined as the difference of I_{DS} between dark and illumination conditions, I_{ph} is equal to $I_{ph\_sp^2} + I_{ph\_sp^3}$. To differentiate these two effects, the photocurrent of the FG/Gr device was measured under laser illumination with a modulated chopper frequency. It is found that a small current oscillates with chopper frequency, superimposing on a larger background current, as depicted in the inset of **Figure 4**a. The black dashed-dotted line represents the dark current. When the chopper blocks the laser, the oscillating current component (due to the trapping in sp^2 domains) disappears immediately; when the laser is totally switched off, the non-oscillating current component (due to the trapping in sp^3 domains) drifts slowly back to the dark current value. Furthermore, no modulated chopper frequency dependence of $I_{ph\_sp^2}$ from 0 to 0.5 Hz was observed (Figure 4a).

The transient photocurrent response to ON/OFF illumination is exhibited in Figure 4b. The FG/Gr shows a larger photocurrent change because of the trapping of photoexcited charge carriers compared to the Gr/Gr. Across the entire tested UV to mid-IR wavelength region, the FG/Gr device consistently shows moderate switching, stability, and reproducibility. When the laser is turned on, the photocurrent reaches its maximum level within 80 ms and decays in 200 ms (Figure S3f, Supporting Information). Despite the high photoresponsivity of our FG/Gr photodetector over a broadband range, we need to point out that the operation speed is not very fast. The reason is the long trapped carrier lifetime in both the sp^2 and the sp^3 domains.[41] The improvement of the operation speed to shorten the lifetime of trapped electrons while maintaining a relatively high responsivity is currently under investigation. With high responsivity and low noise current, the calculated noise equivalent power (NEP) (Figure 4c) reflects the promising prospects of the FG/Gr device in weak light detection. In addition, the peak specific detectivity (D^*) reaches 4×10^{11} Jones (Figure 4d), which is nearly three orders of magnitude larger than that of the Gr/Gr device.

Since the responsivity can be expressed as:

$$R = \eta \frac{\lambda q}{hc} \times \frac{\tau_l}{t_{tr}} \quad (3)$$

where τ_l is the trapped carrier lifetime and t_{tr} is the carrier transit time through the device, we see that $t_{tr} = L^2/\mu_n V_{DS}$. The responsivity against the inverse carrier transit time t_{tr}^{-1} can then be obtained (Figure 4e). The approximately linear scaling of the responsivity with μ_n and L^{-2} illustrates the performance and the relationship between photoconductive gain and channel length of the FG/Gr devices.
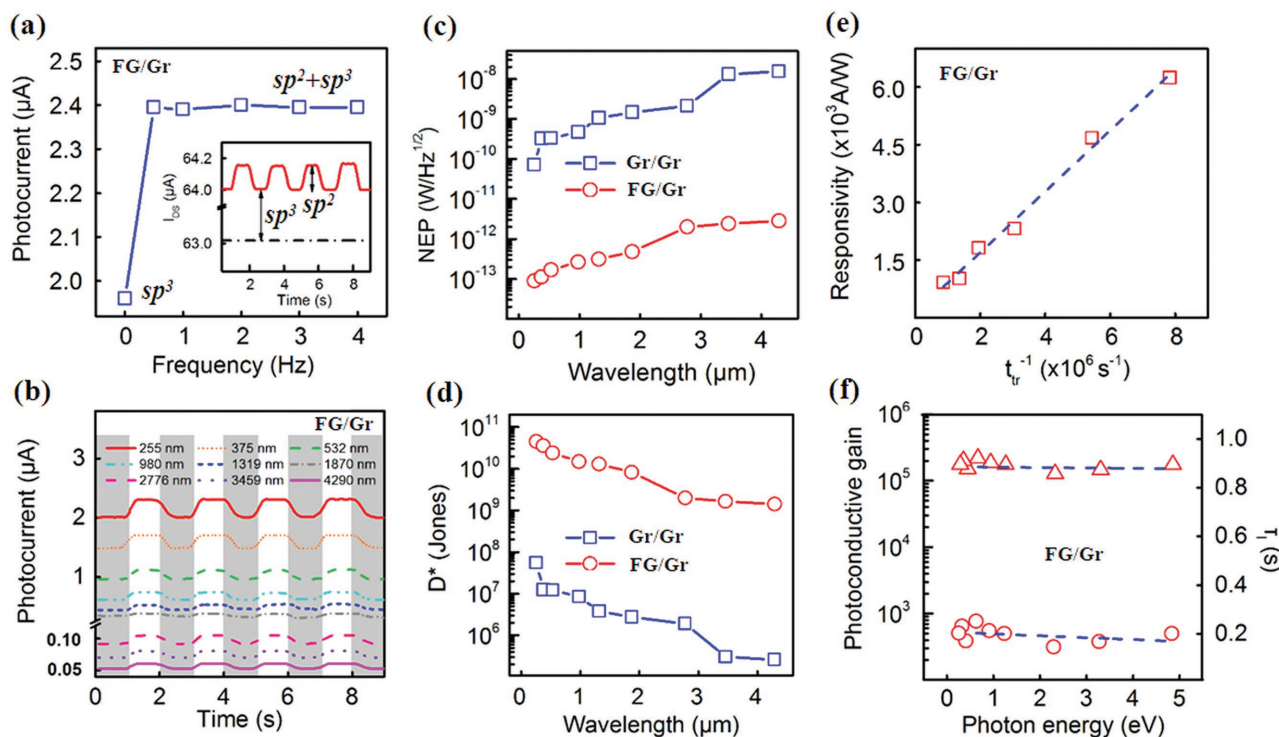
Figure 4. Key metrics of the devices. a) Photocurrent as a function of the chopper frequency. The data point at zero frequency indicates the sp^3 domain photogating. Inset shows that I_{DS} time response in the dark condition (dashed-dotted black line) and under illumination (solid red line), where $\lambda = 532$ nm, $P_{laser} = 198$ µW cm^{-2} and chopper frequency $f = 0.5$ Hz. b) The time response of FG/Gr photodetector at different laser wavelengths, where $V_{DS} = 1$ V and $V_{GS} = 28$ V; lasers were OFF at gray area and ON at white area. c,d) The calculated NEP (c) and D^* (d) of Gr/Gr and FG/Gr photodetector. e) Responsivity as a function of inverse carrier transit time t_{tr}^{-1}. f) The photoconductive gain and carrier lifetime as a function of photon excitation energies. The triangular and circular symbols represent the photoconductive gain and carrier lifetime, respectively. The blue dashed lines in (e) and (f) represent a linear fitting.

Although moderate impact ionization and carrier multiplication have been observed in a quantum-dot-like graphene array structure, where the midgap-state-band electron trapping centers were formed,[8] we believe that there are negligible impact ionization and carrier multiplication effects in our system, which is evidenced by the gain remaining constant with the increase of incident photon energy (Figure 4f). Figure 4f also shows the trapped carrier lifetime as a function of incident photon energy, where the τ_l is about 0.2 s.

The performance of the FG/Gr device shows important advantages over the previous reports, as exhibited in **Figure 5**. The key metrics are also compared in Table S1 in the Supporting Information. Although the responsivity and response time of the FG/Gr photodetector are not the best, consistent performance across the whole tested spectral range from UV to mid-IR has not been reported in the published literature. We notice that the FG could be partially decomposed over time despite its energetic favorability, as indicated by the statistical analysis and error bars in Figure 3. Therefore, the stability of the FG/Gr photodetector has been improved by depositing a thin high-k dielectric material, Al$_2$O$_3$, on top of the device to

passivate the FG. The Al$_2$O$_3$-protected device exhibits stable electrical characteristics. The device was evaluated by re-measuring the photoresponse after exposure to an open-air environment for several months.[42] The device performance was well maintained after that. The responsivity was slightly improved in UV but not in vis and IR, while the response time showed no obvious differences across the tested UV to IR.[43] Furthermore, we believed that the patterning of FG to control the size/shape of sp^2/sp^3 nanodomains would largely influence the device
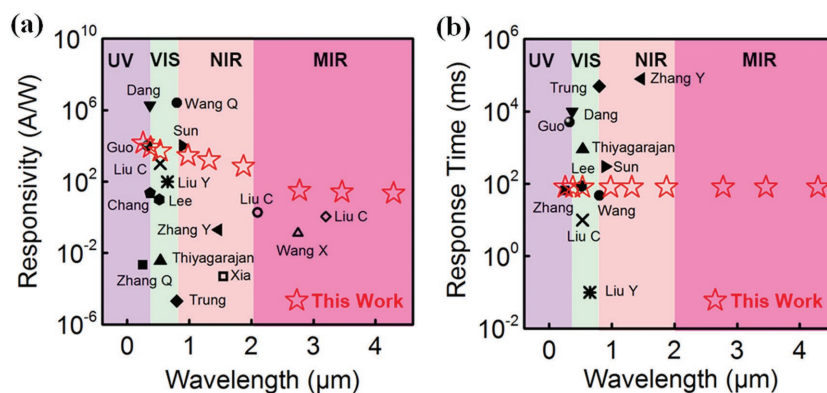

Figure 5. a,b) Responsivity (a) and response time (b) of the FG/Gr photodetector compared to those of related photodetectors reported in the literature.

performance, since the quantum confinement in sp^2 and the localized states at the sp^2/sp^3 edge can be modified. As the FG also possesses the characteristics of a 2D material and can be decomposed in general ambient conditions, it is an alternative candidate for next-generation degradable, flexible, and transparent broadband photodetectors.

In summary, we report a van der Waals heterostructure photodetector consisting of graphene and its fluorine-functionalized derivative that enhances the photoresponse of graphene with broadband sensitivity. The consistent performance of the device shows a broadband photoresponse from UV to mid-IR with high detectivity and moderate switching speed, which can be further improved by engineering the nature of the sp^3 site. The proposed scheme in this work paves the way toward implementation of high-performance broadband graphene-based photodetectors.

Experimental Section

Graphene Growth: Single-crystal graphene was grown in a tube furnace (Thermo Scientific Lindberg/Blue M). Cu foil (Alfa Aesar 46365, thickness of 25 μm) was placed inside the chamber. The chemical vapor deposition (CVD) chamber was evacuated to lower than 0.5 Pa, and then 50 sccm H_2 to 50 Pa was introduced. The Cu foil was annealed at 1060 °C for 100 min. Next, 0.3 sccm O_2 was flowed through the chamber for 10 min to reduce the nucleation density. After this step, single-crystal graphene was grown in 350 sccm H_2 and 0.3 sccm CH_4 for 4 h.[44] The multilayer graphene was grown underneath the first layer of graphene on the Cu foil.

Graphene Transfer: Before transfer, the graphene grown on the reverse side of the Cu foil was etched by O_2 plasma to avoid Cu residues between the topside and reverse side of graphene. After etching, graphene/Cu was spin-coated (with 500 rpm for 5 s and then 4000 rpm for 60 s) by poly(methyl methacrylate) (PMMA) (<100 μm). Then the PMMA/graphene/Cu sample was put into a Cu etching solution ($5H_2O \cdot CuSO_4$:HCl:H_2O = 15.6 g:50 mL:50 mL) for more than 12 h to obtain the PMMA/graphene film. The film was rinsed in deionized (DI) water for 1 min and followed by SC-2 etching solution (H_2O:H_2O_2:HCl = 100 mL:5 mL:5 mL) for 15 min to remove Cu particles. Next, the sample was cleaned in DI water again and placed into SC-1 etching solution (H_2O:H_2O_2:NH_4OH = 100 mL:5 mL:5 mL) to reduce polymer residuals. PMMA/graphene was then transferred onto a SiO_2 substrate. Finally, the PMMA was washed off using dichloromethane (DCM) at 50 °C and isopropyl alcohol (IPA). To minimize the damage and contamination during the process, wet etching, bubble transfer, and RCA were added to the wet-etching transfer process and were compared (Figure S5, Supporting Information). The RCA (Radio Corporation of America) added wet-etching method shows the best graphene quality due to the removal of insoluble inorganic residues and heavy metal contaminants of the RCA cleaning process.

Fluorographene and Characterization: Single-crystal graphene was fluorinated using an inductively coupled plasma (ICP) system (Oxford Instruments) using SF_6 plasma. The FG/Gr heterostructure was fabricated by fluorinating multilayer graphene with SF_6 100 sccm, 5–50 W for 1–120 min. The pressure and gas flow in the ICP reactive chamber were set to 10 mTorr and 100 sccm for the whole study. All the samples were exposed to the plasma only on one side. A Renishaw Invia system with 532 nm laser source was used for Raman characterization. The laser power was ≈1 mW to avoid reduction of fluorine. XPS characterization was conducted using a Thermo Scientific ESCALAB250 Xi system, with a base pressure of 7×10^{-9} mbar. An Al K_α X-ray source (1486.6 eV) was used. The pass energy was 100 eV for survey spectra and 30 eV for core level. The step size was 1 and 0.1 eV, respectively. However, by modifying the C/F ratio x, it was found that x = 3.75 results in the optimized

photodetector performance over other C/F ratios. Hence, the FG with 3.75 C/F ratio was used for the FG/Gr devices. Figure S4a (Supporting Information) illustrates the spectra from the XPS measurements of the graphene and FG, indicating that graphene has been activated by fluorine. Only the very top layer became FG, which was verified by the Raman mapping (Figure S4b, Supporting Information).[45]

Device Fabrication and Characterization: Devices were fabricated on a commercially purchased highly p-doped Si wafer (resistivity of 1–10 Ω cm) with 100 nm SiO_2 layer on top. Gr/Gr and FG/Gr were patterned by photolithography and etched by O_2 plasma to obtain a 150 μm long and 50 μm wide ribbon. The devices were annealed for 120 min at 300 °C under H_2 before all the measurements to remove the residues and contaminants. The photocurrents were measured using an Agilent Semiconductor Analyzer b1500. Nine lasers with wavelengths of 255 nm, 375 nm, 532 nm, 980 nm, 1319 nm, 1870 nm, 2.8 μm, 3.5 μm, and 4.3 μm and irradiance from 4.83 μW cm^{-2} to 11 mW cm^{-2} were used to illuminate the photodetectors. The mid-infrared measurements were conducted at 77 K under 10^{-4} Torr.

Supporting Information

Supporting Information is available from the Wiley Online Library or from the author.

[1] J. P. Clifford, G. Konstantatos, K. W. Johnston, S. Hoogland, L. Levina, E. H. Sargent, *Nat. Nanotechnol.* **2009**, *4*, 40.

[2] J. Liu, D. D. Cannon, K. Wada, Y. Ishikawa, S. Jongthammanurak, D. T. Danielson, J. Michel, L. C. Kimerling, *Appl. Phys. Lett.* **2005**, *87*, 011110.

[3] A. Poglitsch, and 82 others, *Astron. Astrophys.* **2010**, *518*, L2; DOI: 10.1051/0004-6361/201014535.

[4] P. Peumans, A. Yakimov, S. R. Forrest, *J. Appl. Phys.* **2003**, *93*, 3693.

[5] B. L. Carter, E. Shaw, J. T. Olesberg, W. K. Chan, T. C. Hasenberg, M. E. Flatte, *Electron. Lett.* **2000**, *36*, 1301.

[6] J. L. Pau, J. Anduaga, C. Rivera, Á. Navarro, I. Álava, M. Redondo, E. Muñoz, *Appl. Opt.* **2006**, *45*, 7498.

[7] a) C.-H. Liu, Y.-C. Chang, T. B. Norris, Z. Zhong, *Nat. Nanotechnol.* **2014**, *9*, 273; b) H. Yuan, X. Liu, F. Afshinmanesh, W. Li, G. Xu, J. Sun, B. Lian, A. G. Curto, G. Ye, Y. Hikita, Z. Shen, S.-C. Zhang, X. Chen, M. Brongersma, H. Y. Hwang, Y. Cui, *Nat. Nanotechnol.* **2015**, *10*, 707.

[8] B. Y. Zhang, T. Liu, B. Meng, X. Li, G. Liang, X. Hu, Q. J. Wang, *Nat. Commun.* **2013**, *4*, 1811.

[9] J. M. Bioucas-Dias, A. Plaza, presented at 2011 *IEEE Int. Geoscience Remote Sensing Symp. (IGARSS)*, Vancouver, BC, Canada, July **2011**.

[10] J. C. Harsanyi, C. Chang, *IEEE Trans. Geosci. Remote Sens.* **1994**, *32*, 779.

[11] S. N. Chesnokov, D. E. Dolzhenko, I. I. Ivanchik, D. R. Khokhlov, *Infrared Phys. Technol.* **1994**, *35*, 23.

[12] H. Kind, H. Yan, B. Messer, M. Law, P. Yang, *Adv. Mater.* **2002**, *14*, 158.

[13] M. E. Schaffer, P. A. Mitkas, *IEEE J. Sel. Top. Quantum Electron.* **1998**, *4*, 856.

[14] G. Konstantatos, J. Clifford, L. Levina, E. H. Sargent, *Nat. Photonics* **2007**, *1*, 531.

[15] R. Koeppe, A. Neulinger, P. Bartu, S. Bauer, *Opt. Express* **2010**, *18*, 2209.

[16] C. J. Chen, K. K. Choi, W. H. Chang, D. C. Tsui, *Appl. Phys. Lett.* **1998**, *72*, 7.

[17] V. I. Sankin, V. P. Chelibanov, *Phys. Status Solidi* **2001**, *185*, 153.

[18] D. L. Freese, A. Vandenbroucke, D. Innes, F. W. Y. Lau, D. F. C. Hsu, P. D. Reynolds, C. S. Levin, *Med. Phys.* **2015**, *42*, 305.

[19] A. Mäkynen, T. Rahkonen, J. Kostamovaara, *Sens. Actuators, A* **1998**, *65*, 45.

[20] M. B. Gray, D. A. Shaddock, C. C. Harb, H.-A. Bachor, *Rev. Sci. Instrum.* **1998**, *69*, 3755.

[21] L. Vicarelli, M. S. Vitiello, D. Coquillat, A. Lombardo, A. C. Ferrari, W. Knap, M. Polini, V. Pellegrini, A. Tredicucci, *Nat. Mater.* **2012**, *11*, 865.

[22] a) A. K. Geim, K. S. Novoselov, *Nat. Mater.* **2007**, *6*, 183; b) K. S. Kim, Y. Zhao, H. Jang, S. Y. Lee, J. M. Kim, K. S. Kim, J.-H. Ahn, P. Kim, J.-Y. Choi, B. H. Hong, *Nature* **2009**, *457*, 706.

[23] a) K. S. Novoselov, A. K. Geim, S. V. Morozov, D. Jiang, M. I. Katsnelson, I. V. Grigorieva, S. V. Dubonos, A. A. Firsov, *Nature* **2005**, *438*, 197; b) A. H. C. Neto, F. Guinea, N. M. R. Peres, K. S. Novoselov, A. K. Geim, *Rev. Mod. Phys.* **2009**, *81*, 109.

[24] L. Ju, B. Geng, J. Horng, C. Girit, M. Martin, Z. Hao, H. A. Bechtel, X. Liang, A. Zettl, Y. R. Shen, F. Wang, *Nat. Nanotechnol.* **2011**, *6*, 630.

[25] M. Furchi, A. Urich, A. Pospischil, G. Lilley, K. Unterrainer, H. Detz, P. Klang, A. M. Andrews, W. Schrenk, G. Strasser, T. Mueller, *Nano Lett.* **2012**, *12*, 2773.

[26] X. Gan, R.-J. Shiue, Y. Gao, I. Meric, T. F. Heinz, K. Shepard, J. Hone, S. Assefa, D. Englund, *Nat. Photonics* **2013**, *7*, 883.

[27] W. Zhang, C.-P. Chuu, J.-K. Huang, C.-H. Chen, M.-L. Tsai, Y.-H. Chang, C.-T. Liang, Y.-Z. Chen, Y.-L. Chueh, J.-H. He, M.-Y. Chou, L.-J. Li, *Sci. Rep.* **2014**, *4*, 3826.

[28] G. Konstantatos, M. Badioli, L. Gaudreau, J. Osmond, M. Bernechea, F. P. G. de Arquer, F. Gatti, F. H. L. Koppens, *Nat. Nanotechnol.* **2012**, *7*, 363.

[29] a) O. Leenaerts, H. Peelaers, A. D. Hernández-Nieves, B. Partoens, F. M. Peeters, *Phys. Rev. B* **2010**, *82*, 195436; b) H. Şahin, M. Topsakal, S. Ciraci, *Phys. Rev. B* **2011**, *83*, 115432.

[30] J. O. Sofo, A. M. Suarez, G. Usaj, P. S. Cornaglia, A. D. Hernández-Nieves, C. A. Balseiro, *Phys. Rev. B* **2011**, *83*, 081411.

[31] Z. H. Ni, L. A. Ponomarenko, R. R. Nair, R. Yang, S. Anissimova, I. V. Grigorieva, F. Schedin, P. Blake, Z. X. Shen, E. H. Hill, K. S. Novoselov, A. K. Geim, *Nano Lett.* **2010**, *10*, 3868.

[32] J.-A. Yan, L. Xian, M. Y. Chou, *Phys. Rev. Lett.* **2009**, *103*, 086802.

[33] C.-T. Chien, S.-S. Li, W.-J. Lai, Y.-C. Yeh, H.-A. Chen, I. S. Chen, L.-C. Chen, K.-H. Chen, T. Nemoto, S. Isoda, M. Chen, T. Fujita, G. Eda, H. Yamaguchi, M. Chhowalla, C.-W. Chen, *Angew. Chem.* **2012**, *124*, 6766.

[34] a) K. Thiyagarajan, A. Ananth, B. Saravanakumar, Y. S. Mok, S.-J. Kim, *Carbon* **2014**, *73*, 25; b) K. Thiyagarajan, B. Saravanakumar, S.-J. Kim, *ACS Appl. Mater. Interfaces* **2015**, *7*, 2171.

[35] R. R. Nair, W. Ren, R. Jalil, I. Riaz, V. G. Kravets, L. Britnell, P. Blake, F. Schedin, A. S. Mayorov, S. Yuan, M. I. Katsnelson, H.-M. Cheng, W. Strupinski, L. G. Bulusheva, A. V. Okotrub, I. V. Grigorieva, A. N. Grigorenko, K. S. Novoselov, A. K. Geim, *Small* **2010**, *6*, 2877.

[36] L. Britnell, R. M. Ribeiro, A. Eckmann, R. Jalil, B. D. Belle, A. Mishchenko, Y.-J. Kim, R. V. Gorbachev, T. Georgiou, S. V. Morozov, A. N. Grigorenko, A. K. Geim, C. Casiraghi, A. H. C. Neto, K. S. Novoselov, *Science* **2013**, *340*, 1311.

[37] X. Cai, A. B. Sushkov, R. J. Suess, M. M. Jadidi, G. S. Jenkins, L. O. Nyakiti, R. L. Myers-Ward, S. Li, J. Yan, D. K. Gaskill, T. E. Murphy, H. D. Drew, M. S. Fuhrer, *Nat. Nanotechnol.* **2014**, *9*, 814.

[38] N. Kurra, V. S. Bhadram, C. Narayana, G. U. Kulkarni, *Nanoscale* **2013**, *5*, 381.

[39] N. M. Gabor, J. C. W. Song, Q. Ma, N. L. Nair, T. Taychatanapat, K. Watanabe, T. Taniguchi, L. S. Levitov, P. Jarillo-Herrero, *Science* **2011**, *334*, 648.

[40] M. M. Furchi, D. K. Polyushkin, A. Pospischil, T. Mueller, *Nano Lett.* **2014**, *14*, 6165.

[41] a) A. Cortijo, M. A. H. Vozmediano, *Nucl. Phys. B* **2007**, *763*, 293; b) Y. A. Sitenko, N. D. Vlasii, *Nucl. Phys. B* **2007**, *787*, 241.

[42] Y. Xu, A. Ali, K. Shehzad, N. Meng, M. Xu, Y. Zhang, X. Wang, C. Jin, H. Wang, Y. Guo, Z. Yang, B. Yu, Y. Liu, Q. He, X. Duan, X. Wang, P.-H. Tan, W. Hu, H. Lu, T. Hasan, *Adv. Mater. Technol.* **2016**, *2*, 1600241.

[43] X. Wan, Y. Xu, H. Guo, K. Shehzad, A. Ali, Y. Liu, J. Yang, D. Dai, C.-T. Lin, L. Liu, H.-C. Cheng, F. Wang, X. Wang, H. Lu, W. Hu, X. Pi, Y. Dan, J. Luo, T. Hasan, X. Duan, X. Li, J. Xu, D. Yang, T. Ren, B. Yu, unpublished.

[44] P. Zhao, Y. Cheng, D. Zhao, K. Yin, X. Zhang, M. Song, S. Yin, Y. Song, P. Wang, M. Wang, Y. Xia, H. Wang, *Nanoscale* **2016**, *8*, 7646.

[45] Q. Li, H. Chou, J.-H. Zhong, J.-Y. Liu, A. Dolocan, J. Zhang, Y. Zhou, R. S. Ruoff, S. Chen, W. Cai, *Nano Lett.* **2013**, *13*, 486.